JOURNAL OF SPACECRAFT AND ROCKETS
Vol. 44, No. 3, May–June 2007

Correlation and Error Metrics for Plant Identification of On-Orbit Space Structures

Steven A. Lane* and Seth L. Lacy†
U.S. Air Force Research Laboratory, Kirtland Air Force Base, New Mexico 87117
and
Vít Babuška‡ and Delano Carter§
General Dynamics–Advanced Information Systems, Albuquerque, New Mexico, 87102

DOI: 10.2514/1.24583

In plant identification and modeling efforts, metrics are needed to quantitatively compare measured data to numeric models. Quantitative metrics broadly fall into five categories: performance metrics, correlation metrics, error metrics, data quality metrics, and model interpretation metrics. This paper describes the utility of frequency response function correlation and error metrics for plant identification, particularly for complex space structures. Three correlation metrics and three error metrics are discussed. Multiple-input, multiple-output extensions to the correlation metrics are presented and their application is demonstrated on data collected from spacecraft-representative structures.

Nomenclature

$G_{m,n}(k)$	=	identified model complex response at frequency $f(k)$
$\hat{G}_{m,n}(k)$	=	measured complex response at frequency $f(k)$
K	=	number of frequency points in a frequency response function
M	=	total number of output channels
m	=	output channel
N	=	total number of input channels
n	=	input channel
$U(k)$	=	matrix of left singular vectors associated with the nonzero singular values of the identified model complex response at frequency $f(k)$
$\hat{U}(k)$	=	matrix of left singular vectors associated with the nonzero singular values of the measured complex response at frequency $f(k)$
$V(k)$	=	matrix of right singular vectors associated with the nonzero singular values of the identified model complex response at frequency $f(k)$
$\hat{V}(k)$	=	matrix of right singular vectors associated with the nonzero singular values of the measured complex response at frequency $f(k)$
$\Delta(k)$	=	scalar value representing the parametric multiplicative uncertainty of the given system model at frequency $f(k)$
σ	=	system singular values
$\bar{\sigma}$	=	maximum singular value
$\underline{\sigma}$	=	minimum singular value
H	=	complex conjugate transpose
$*$	=	complex conjugate
$:$	=	subscript to denote all rows or columns of a matrix
$\lvert\cdots\rvert$	=	denotes absolute value or magnitude
$\lVert\cdots\rVert$	=	denotes Euclidean vector norm; 2-norm
$\lVert\cdots\rVert_{\text{Fro}}$	=	denotes matrix Frobenius norm; square root of the sum of the squared element magnitudes

Presented as Paper 2012 at the 46th AIAA/ASME/ASCE/AHS/ASC Structures, Structural Dynamics and Materials Conference, Austin, TX, 21 April 2005; received 12 April 2006; revision received 14 August 2006; accepted for publication 19 August 2006.

*Research Aerospace Engineer, Space Vehicles Directorate, Senior AIAA Member.
†Aerospace Engineer, Space Vehicles Directorate, Senior AIAA Member.
‡Research Engineer, General Dynamics–Advanced Information Systems, National Systems Group, AIAA Associate Fellow.
§Aerospace Engineer, General Dynamics–Advanced Information Systems, National Systems Group, AIAA Member.

I. Introduction

THE U.S. Air Force Research Laboratory (AFRL) is actively engaged in research and development efforts to improve the accuracy and to expand the frequency bandwidth of test-verified structural dynamic modeling techniques for complex, precision space structures. The impetus behind these efforts is the projection that some future spacecraft may be too large and compliant to undergo system-level testing in their deployed configuration before launch. Because system-level, integrated testing and validation would not be feasible in a 1*g* environment, designers must rely on subcomponent model validation. This represents a dramatically new paradigm for the aerospace industry. For this paradigm to be realized, current modeling and test methods need to be advanced. First, modeling approaches need to be able to predict subcomponent and system-level behavior accurately over two or three decades, even for modally dense systems. Such modeling approaches include deterministic methods (i.e., finite elements, boundary elements), nondeterministic methods (i.e., statistical energy analysis, energy flow method), and hybrid methods that combine the two approaches. Second, methods to track subcomponent model uncertainty and bound system-level model uncertainty must be developed. A key task for this is to understand relevant sources of uncertainty and how they propagate through the modeling process. Third, methods to test complex structures to relatively high frequency must be developed so that measurements used to validate subcomponent models are reliable. Typically, modal testing is used to validate models of low modal density, but as the modal density increases and substructure coupling becomes significant, the metrics used to measure data quality offer less insight. A final critical area is development of improved methods to create models from "system identification" techniques.

Finite element modeling (FEM) became widely accepted for modeling structural dynamics in the 1960s with the development of computers [1–3]. FEM has been incrementally improved, with standard packages such as NASTRAN, ANSYS, and ABAQUS representing the current state-of-the-art in deterministic modeling capabilities. The accuracy of such modeling approaches is limited by the underlying assumptions on damping mechanisms, joints/

connections, boundary conditions, loading conditions, and material properties. Recent research has focused on parametric uncertainty and attempting to quantify sensitivity using Monte Carlo simulations [4–6]. Modeling of high frequency and statistical behavior of structures has also been an area of active research since the 1950s [7,8]. Recently, hybrid modeling tools were developed by the AFRL and small businesses that bridged the midfrequency gap between low-frequency deterministic methods and high-frequency statistical methods [9–11].

Modeling is not only germane to the early design stages of space structures, but is essential to ensuring their performance on orbit. It is anticipated that initial models of spacecraft will be validated using data measured after on-orbit deployment. This Earth-to-space system identification process has a few challenges: sensors and actuators cannot be repositioned or replaced; changes to the dynamic range, sensitivity, and sensor conditioning become more difficult; and there is an inherent time lag between data collection and analysis. Test and analysis time become an even greater program cost; data quality, model correlation, and model uncertainty need to be quickly and accurately characterized. Models are necessary for designing deployment, maneuvering, and vibration suppression controllers. Control systems will be critical to mission performance, therefore controllers must provide robust stability and robust performance, and may need to autonomously adapt to changes in the system. Structures such as space telescopes would be folded for launch, deployed on orbit, and then controlled to nanometer level tolerances. Bandwidth requirements are driven by mission needs for on-orbit feedback control for pointing, tracking, jitter suppression, vibration isolation, active damping, or wave front error control. Controllers must be robust to changes in the disturbance and variations of the spacecraft over time.

This paper evaluates frequency response function (FRF) correlation and error metrics for assessing identified plant models of complex space structures. In the next section, terms are defined and characteristics of metrics are discussed. This is followed by a discussion of the plant identification process that has been used at AFRL to identify plant models for complex structures including the SUITE platform [12,13], and the deployable optical telescope (DOT) testbed [14]. Three FRF correlation metrics and error metrics are discussed, which include multi-input, multi-output (MIMO) extensions to previously published single-input, single-output (SISO) metrics. Next, the metrics are applied to data and the corresponding models of spacecraft-representative structures to demonstrate utility. The paper concludes with observations on the general use and applicability of correlation and error metrics in the plant identification process.

II. Terms and Metric Characteristics

The term system identification is interpreted differently by structural dynamicists and control engineers. For structural dynamicists, system identification generally implies synthesizing second order models from modal test data. For control engineers, system identification implies defining parameters in a model's structure to determine the input-output properties of a system with the intent of using the results for control system design, open-loop, and closed-loop analyses. Because this paper is concerned with the latter interpretation, the term "plant identification" is used in lieu of system identification to remove any possible ambiguity. The term "modal identification" will be used for the former interpretation.

In plant identification and modeling efforts, metrics are needed to quantitatively compare data and models. Quantitative metrics broadly fall into five categories:

1) Performance metrics: These capture specific response quantities of hardware or a system model, such as wave front error and line of sight jitter. The calculation of performance metrics requires a system representation (model and measurements) as well as input properties.

2) Correlation metrics: In modal identification, correlation metrics such as cross-orthogonality [15] are used. In plant identification, metrics for comparing FRFs are employed because of the limited number of sensors and different identification and modeling objectives. The FRFs can be generated from models or from experimental data. Correlation metrics used for plant identification are also applicable to modal identification.

3) Error metrics: In plant identification, model fit errors are of interest, particularly if the plant models will be used in control system design and/or analyses. Frequency-domain uncertainties and stability margins are used in robust control theory and classical SISO control analysis. Model fit errors can be used to define these bounds.

4) Data quality metrics: These metrics describe the "quality" of measured data. This includes measures of uncertainty as well as characterizations of system behavior, such as nonlinearity.

5) Model interpretation metrics: These are quantities that identify characteristics of plant models, such as dominant modes and damping characteristics.

The utility of quantitative metrics depends on the following factors:

1) Applicability: The metric must be consistent with the planned use of the model. Because the plant identification exercise is not an end in itself, the metric must describe the quality of the model in the appropriate context.

2) Insight: The metric must provide information about the deficiencies of the model in a form that provides insight and guidance to the engineer in updating or tuning the model. It must illuminate deficiencies without overwhelming the engineer with incorrect information that falsely indicates modeling deficiencies.

3) Consistency: Tuning or synthesis algorithms that are consistent with the metric must exist and be practical. Not all evaluation metrics make good cost functions in identification algorithms for lightly damped, modally dense systems because the computational expense is prohibitive. An approximation of the metric in a model-tuning algorithm, or clever use of weighting matrices to appropriately approximate the metric is often required.

III. Plant Identification

The plant identification process used to obtain state-space models is shown graphically in Fig. 1. The metrics discussed herein were used to assess the quality of the identified plant models by comparing the measured and model-generated FRFs. The process in Fig. 1 has been used to identify high-order models of precision structures including the AFRL deployable optical telescope (DOT) testbed and other representative space structures. Similar to the approach described by Jacques [16], this process divides the identification problem into two stages: plant synthesis and plant model tuning.

The first and most critical step of plant identification is collecting data from the structure or system to be modeled. The data collection process determines the bandwidth of the model, frequency resolution of the model, and ultimately the quality of the model. Time-domain data can be used to synthesis time-domain models, or can be averaged, converted to the frequency domain, and used to develop frequency-domain models as shown in Fig. 1. Averaging is attractive in that the signal-to-noise ratio (SNR) is improved.

After complex frequency response function representations of the system transfer functions are obtained, prescaling of the data can be applied to aid subsequent model synthesis and tuning. When possible, measured frequency response data are not subdivided into frequency bands as indicated in Fig. 1. Although frequency band division reduces the computational burden in the plant synthesis step, it increases the difficulty of the model-tuning effort. Frequency band division may be necessary to model low amplitude response if there is a large variation in amplitude of the system over the desired bandwidth.

The kernel in the plant synthesis step can be any frequency-domain subspace technique (or time-domain method). With frequency-domain methods, data from multiple individual data collection experiments can be assembled to generate a high-bandwidth FRF matrix. Band-limited FRFs generated in separate tests can be "stitched" together to form the full-bandwidth FRF matrix. Also, the excitation signals can be tailored to account for system properties. For example, the input amplitude can be scaled to

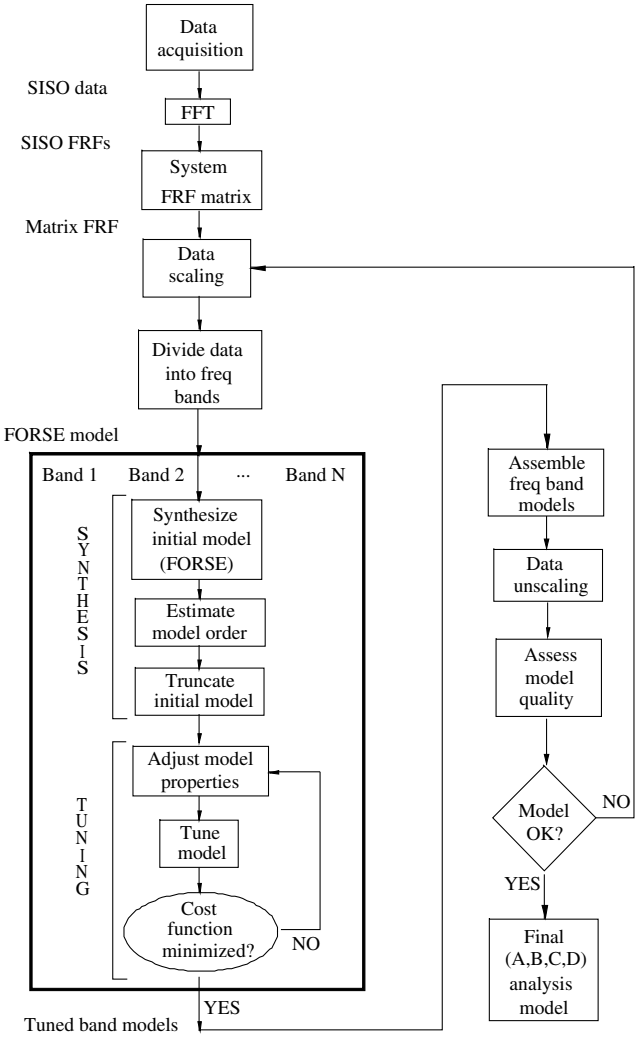

Fig. 1 Plant identification process.

obtain good signal-to-noise in and around system zeros, and to avoid sensor saturation around system poles. Frequency data need not be uniformly spaced. Often logarithmic frequency spacing is used when measurements are collected over large bandwidths. For very high-order systems, models can be identified in separate frequency bands and later combined to form a single model. The specific subspace method adopted in this effort was the FORSE [17] algorithm as realized in an almost commercial-off-the-shelf (COTS) version of the DynaMod software.[¶] Model order is often determined based on the magnitude of the Hankel singular values. Model-order reduction can be achieved using truncation or residualization [18].

The plant tuning step is important because it allows the engineer to assess and adjust the synthesized model. Deficiencies in the synthesized plant model can be corrected through tuning with appropriate cost functions and weighting matrices. For example, plant synthesis algorithms have demonstrated difficulty fitting MIMO models containing zeros at the origin (or even low amplitude response at low frequency). A model can be improved in the low-frequency band by model tuning with appropriate weighting matrices. Plant tuning also is used to realize optimal models for nonconvex cost functions such as maximum likelihood. Plant model tuning is a time consuming process that involves nonlinear optimization combined with engineering judgment and experience.

Once the tuning process is complete, i.e., the chosen cost function has been sufficiently optimized, the model is assembled and scaling is removed to provide a representation of the plant. It is here that frequency response function correlation and error metrics are helpful in assessing the quality of the model. If model-data error proves to be too large, then the paradigm is repeated using a variant of weighting matrices, optimization approach, possibly a different initial model, and incorporating other knowledge gained from the previous iteration. In the end, models must be checked for stability and if they are reasonable. It is often that numeric algorithms yield models that fit, but require unreasonable model orders, damping values, or attempt to fit data of poor quality (low coherence).

[¶]http://www.mide.com/products.html#dynamod.

IV. Frequency Response Function Correlation and Error Metrics

Correlation metrics are used more regularly in modal identification than plant identification. This is a result of the different objectives involved. Because modal identification involves many sensors (necessary for mode-shape identification), the concept of correlation is natural. Many frequency-domain correlation metrics originated from the modal identification field where quantities such as cross-orthogonality and the modal assurance criterion are used to assess the global "sameness" of mode-shape vectors (comparing the fitted model to the measured data). The same concept can be used in the frequency domain with different independent parameters, such as frequency, output sensors, and input sensors (or actuators).

A. Correlation Metrics

The modal assurance criteria (MAC) is a tool commonly used to assess model-data correlation. Analytic modal descriptions of systems can have an infinite number of modes, but practical limits on the number of sensors and actuators used in testing limits the number of modes that can be extracted from test data. Ideally, the mode shapes extracted from test data and computed from a corresponding model yield an orthonormal basis set and are uncorrelated. However, to get an accurate estimate of a mode-shape, it must be spatially sampled at a sufficient resolution or the experimental and analytic mode shapes will not be orthogonal. Consider a system model with R mode shapes defined here as ϕ_r where $r = 1{:}R$. Now assume that S modes are extracted from test data of the corresponding system and are denoted as ϕ_s where $s = 1{:}S$. The modal assurance criteria can be computed as (assuming ϕ_r and ϕ_s are column vectors):

$$\mathrm{MAC}\,(r,s) = \frac{(\phi_r^H \phi_s)(\phi_s^H \phi_r)}{(\phi_r^H \phi_r)(\phi_s^H \phi_s)} \tag{1}$$

To indicate good model-data correlation, the diagonal elements of the MAC should be near unity and off-diagonal elements should be small. Obtaining such correlation over wide bandwidths can be difficult in practice, and may not be as useful for controller development as frequency response based metrics. This is especially true for complex, modally dense systems such as large space structures.

Prior work by Dascotte and Strobbe [19], Pascual et al. [20], Fotsch and Ewins [21], and Heylen and Avitabile [22] describes various single-input, multiple-output (SIMO) FRF correlation metrics and gives application examples. The metrics are similar and are based on the concept of an inner product of a vector space. They describe the degree of similarity between measured FRFs and model-generated FRFs in a geometric sense. Specifically, two unit vectors in a complex vector space of arbitrary dimension are parallel if their inner product is unity. The closer to unity, the more correlated are the vectors, as illustrated in Fig. 2. Therefore, good model and data matching (correlation) is indicated with values near unity. If the vectors are instead orthogonal, the correlation metric is zero.

The three correlation metrics discussed in this paper are 1) frequency response assurance criterion (FRAC)[22], 2) cross signature assurance criterion (CSAC) [19] (closely related to frequency-domain assurance criteria [20]), and 3) cross signature scale factor (CSSF) [19].

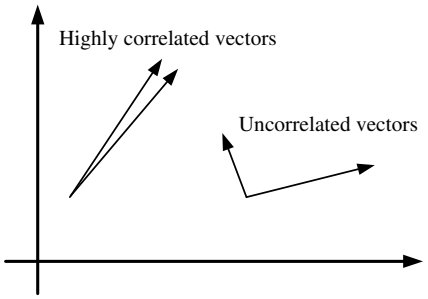

Fig. 2 Vector correlation concept.

1. Frequency Response Assurance Criterion

The FRAC has been discussed in various papers on modal testing applications [21,22]. It is defined as

$$\text{FRAC}_{m,n} = \frac{|\hat{G}_{m,n}^H G_{m,n}|^2}{(G_{m,n}^H G_{m,n})(\hat{G}_{m,n}^H \hat{G}_{m,n})} = \frac{|\sum_{k=1}^K \hat{G}_{m,n}^*(k) G_{m,n}(k)|^2}{\left[\sum_{k=1}^K G_{m,n}^*(k) G_{m,n}(k)\right]\left[\sum_{k=1}^K \hat{G}_{m,n}^*(k) \hat{G}_{m,n}(k)\right]} \tag{2}$$

The FRAC is a scalar value that represents the correlation of two SISO FRFs across frequency. Perfect correlation of FRFs is indicated by FRAC = 1. The FRAC is independent of FRF scaling, so it is insensitive to a constant gain error between FRFs. It is also insensitive to constant phase shifts per channel (input-to-output transfer path) over frequency between two FRFs, including 180 deg shifts. Because the FRAC essentially averages over frequency, it only gives an indication of differences. Gross mismatches in small frequency bands where the FRF magnitude is comparatively high lead to low FRAC values.

The FRAC is a SISO metric, but it can be generalized. One way of applying the FRAC to MIMO systems is to form a matrix of all the SISO FRAC values:

$$[\text{FRAC}] = \begin{bmatrix} \text{FRAC}_{1,1} & \text{FRAC}_{1,2} & \cdots & \text{FRAC}_{1,N} \\ \text{FRAC}_{2,1} & \text{FRAC}_{2,2} & & \text{FRAC}_{2,N} \\ \vdots & & \ddots & \vdots \\ \text{FRAC}_{M,1} & \text{FRAC}_{M,2} & \cdots & \text{FRAC}_{M,N} \end{bmatrix} \tag{3}$$

This permits comparisons of multiple SISO FRACs and can illuminate potential problems with actuators, sensors, or specific structural components (e.g., joints). A second MIMO extension is to calculate FRACs for the principal gains of a MIMO system. This version does not provide as much insight as the former version because the transformation into principal gain space obscures the input/output relationships.

2. Cross Signature Assurance Criterion

The CSAC [19] is defined as:

$$\text{CSAC}_n(k) = \frac{|\hat{G}_{:,n}^H(k) G_{:,n}(k)|^2}{[G_{:,n}^H(k) G_{:,n}(k)][\hat{G}_{:,n}^H(k) \hat{G}_{:,n}(k)]} = \frac{|\sum_{m=1}^M \hat{G}_{m,n}^*(k) G_{m,n}(k)|^2}{\left[\sum_{m=1}^M G_{m,n}^*(k) G_{m,n}(k)\right]\left[\sum_{m=1}^M \hat{G}_{m,n}^*(k) \hat{G}_{m,n}(k)\right]} \tag{4}$$

This CSAC is the magnitude-squared of the dot-product of two complex unit vectors created from the columns of an FRF matrix at each frequency. It is a measure of the spatial shape correlation of the FRFs using a common set of sensors for a specific input as a function of frequency. The "unit vectors" are created by scaling the FRF columns by their magnitudes making this metric insensitive to uniform scale factor errors. The metric will be sensitive to individual channel scale factor errors. In this case, the CSAC will be uniformly low across all frequencies. This metric is insensitive to a constant phase shift for all channels and over frequency between the two FRFs.

The CSAC is a SIMO or multi-input, single-output (MISO) criterion only; it is not a true MIMO criterion, and is meaningless for SISO systems. Possible values range from zero to one, with unity indicating perfect correlation. Because the CSAC is a direction criterion, it is possible to get perfect correlation when two vectors are 180 deg out of phase, or when there is a constant phase shift for all channels and over frequency between the two FRFs. Squaring the magnitude has a reducing effect on the value, so this metric is comparatively strict. Because of the normalization of the "vectors", the CSAC criterion contains no amplitude information. It must be used in conjunction with another criterion that provides information about the magnitudes of the vectors. For this, the CSSF metric or an error metric can be used.

There is no unique MIMO extension to the CSAC, but a number of options exist:

1) Calculate column and row CSACs: This yields $N \times M$ CSAC plots. This version is useful because it shows channel sensitivities without distorting the data space. At resonance frequencies, the column CSAC approximates the modal assurance criterion and is a measure of mode-shape correlation. The row CSAC describes the degree of correlation of FRF rows.

2) Vectorize the FRF matrices in Eq. (4): This converts a MIMO FRF matrix into a column vector that can be used in Eq. (4). Some channel-specific insight is lost. This implementation has the same sensitivities and insensitivities discussed for the SIMO or MISO version. Replacing the vector norms in Eq. (4) with matrix Frobenius norms gives

$$\text{VCSAC}(k) = \frac{\left|\sum_{n=1}^N \hat{G}_{:,n}^H(k) G_{:,n}(k)\right|^2}{\|G(k)\|_{\text{Fro}}^2 \|\hat{G}(k)\|_{\text{Fro}}^2} \tag{5}$$

The vectorized CSAC (VCSAC) is a real vector and all entries are unity when FRFs are perfectly correlated. The VCSAC has the same sensitivities and insensitivities discussed for the SIMO version.

3) Create a principal gain CSAC (PGCSAC): This option extends the geometric (i.e., vector dot-product) interpretation of the SIMO CSAC. The geometrically inspired MIMO extension of the SIMO CSAC compares two hyper-surfaces or subspaces. The shape correlation of these hyper-surfaces is captured by dot products of the singular vectors of G and $\hat{G}$ associated with nonzero singular values. These could be the left singular vectors (i.e., the basis for the range spaces of G and $\hat{G}$) or the right singular vectors (i.e., the basis for the domain spaces of G and $\hat{G}$). Singular vectors are orthonormal, so no additional scaling is necessary. However, the singular value decomposition (SVD) is a transformation into principal gain space where it is better to use the left and right singular vectors simultaneously. The principal gain CSAC shall be defined as

$$\text{PGCSAC}(k) = \text{diag}(|C(k)|^2) \tag{6}$$

where

$$C(k) = [\hat{G}(k)\hat{G}^H(k)]^{-1/2}[\hat{G}(k)G^H(k)][G(k)G^H(k)]^{-1/2} = \hat{U}(k)[\hat{V}(k)_{(:,1:M)}]^H V(k)_{(:,1:M)} U^H(k) \tag{7}$$

for "wide" matrices, and

$$C(k) = [\hat{G}^H(k)\hat{G}(k)]^{-1/2}[\hat{G}^H(k)G(k)][G^H(k)G(k)]^{-1/2} = \hat{V}(k)[\hat{U}(k)_{(:,1:N)}]^H U(k)_{(:,1:N)} V^H(k) \tag{8}$$

for "tall" matrices. See the Appendix for the algebraic details for the derivation of Eqs. (7) and (8). The PGCSAC is a real vector at each frequency and all entries are unity when FRFs are perfectly correlated. If some PGCSAC values are low at a particular frequency, there are principal directions in which the correlation is poor. This

usually is caused by low SNR. The PGCSAC has the same sensitivities and insensitivities discussed for the SIMO version.

3. Cross Signature Scale Factor

The SIMO CSSF is also defined in Dascotte and Strobbe [19]. It is given as

$$\mathrm{CSSF}_n(k) = \frac{2|\hat{G}^H_{:,n}(k)G_{:,n}(k)|}{[G^H_{:,n}(k)G_{:,n}(k)] + [\hat{G}^H_{:,n}(k)\hat{G}_{:,n}(k)]} = \frac{2|\sum_{m=1}^{M}\hat{G}^*_{m,n}(k)G_{m,n}(k)|}{\left[\sum_{m=1}^{M}G^*_{m,n}(k)G_{m,n}(k)\right] + \left[\sum_{m=1}^{M}\hat{G}^*_{m,n}(k)\hat{G}_{m,n}(k)\right]} \quad (9)$$

assuming colinearity between $G(k)$ and $\hat{G}(k)$. This metric is described as a measure of amplitude correlation between FRFs at each frequency. Like the CSAC, it is real valued and at most a SIMO metric. Values of the CSSF range from zero to one, with unity indicating a perfect match between the FRFs. It is understood to be sensitive to discrepancies in FRF amplitudes (scale factors). It is possible to get perfect correlation with a constant phase shift for all channels and over frequency between the two FRFs. Together, the CSAC and the CSSF metrics are referred to as "cross signature correlation" functions. Whereas the CSAC obviously is an inner product of two vectors, the origins of the CSSF are not as obvious and are not given in Dascotte and Stobbe [19].

The CSSF is not independent of the CSAC; in fact, it is a scaled version of the CSAC. With some algebraic dexterity (see the Appendix), the CSSF expression becomes

$$\mathrm{CSSF}_n(k) = \frac{2|\hat{G}^H_{:,n}(k)G_{:,n}(k)|}{[G^H_{:,n}(k)G_{:,n}(k)] + [\hat{G}^H_{:,n}(k)\hat{G}_{:,n}(k)]} = \frac{2\|\hat{G}^H_{:,n}(k)\|\|G_{:,n}(k)\|}{\|G_{:,n}(k)\|^2 + \|\hat{G}_{:,n}(k)\|^2}\sqrt{\mathrm{CSAC}_n(k)} \quad (10)$$

The CSSF essentially reduces to the CSAC for normalized frequency response data sets. Squaring the CSSF for normalized frequency response data sets would yield the exact CSAC result. A truly complementary amplitude correlation metric to the CSAC would not include the CSAC in the expression. Without relying on the colinearity assumption, the CSSF expression becomes

$$\mathrm{CSSF}\,2_n(k) = \frac{2\|G_{:,n}(k)\|\|\hat{G}_{:,n}(k)\|}{\|G_{:,n}(k)\|^2 + \|\hat{G}_{:,n}(k)\|^2} \quad (11)$$

which is independent of and complementary to the CSAC.

There is no unique MIMO extension for the CSSF. Because the role of the CSSF is to provide information about the magnitudes of the FRF matrix vectors, any of the principal gain error metrics can be used. Like the CSAC, a number of options exist for extending the SIMO CSSF expressions to the MIMO case:

1) Calculate the CSSF for each input and output; this is analogous to the column and row CSACs.

2) Vectorize the FRF matrices in Eq. (9); this converts a MIMO FRF matrix into a SIMO-like FRF vector. It is a direct matrix analogue of the SIMO CSSFs. The analogue of Eq. (9) is

$$M\mathrm{CSSF}(k) = \frac{2\left|\sum_{n=1}^{N}\hat{G}^*_{:,n}(k)G_{:,n}(k)\right|}{\|G(k)\|^2_{\mathrm{Fro}} + \|\hat{G}(k)\|^2_{\mathrm{Fro}}} \quad (12)$$

whereas the analogue of Eq. (11) is

$$M\mathrm{CSSF2}(k) = \frac{2\|G(k)\|_{\mathrm{Fro}}\|\hat{G}(k)\|_{\mathrm{Fro}}}{\|G(k)\|^2_{\mathrm{Fro}} + \|\hat{G}(k)\|^2_{\mathrm{Fro}}} \quad (13)$$

3) Define a principal gain CSSF; this is analogous to the principal gain CSAC. Conceptually, the principal gain CSSF compares the sizes of the principal gain hyper-surfaces. A PGCSSF based on extending Eq. (10) is

$$\mathrm{PGCSSF}_i(k) = \frac{2\sigma^G_i(k)\sigma^{\hat{G}}_i(k)}{[\sigma^G_i(k)]^2 + [\sigma^{\hat{G}}_i(k)]^2}\sqrt{\mathrm{CSAC}_i(k)} \quad \text{for } i = 1,\ldots,\min(M,N) \quad (14)$$

and the MIMO extension of Eq. (11) is

$$\mathrm{PGCSSF}\,2_i(k) = \frac{2\sigma^G_i(k)\sigma^{\hat{G}}_i(k)}{[\sigma^G_i(k)]^2 + [\sigma^{\hat{G}}_i(k)]^2} \quad \text{for } i = 1,\ldots,\min(M,N) \quad (15)$$

The PGCSSF2 is a real vector at each frequency. The FRFs are perfectly correlated when the PGCSSF2 entries are all unity. If one or more of the elements are small, there is a gain mismatch in one of the principal directions. The causes are the same as those that create a low PGCSAC, primarily low signal-to-noise. Both PGCSSFs have the same sensitivities and insensitivities discussed for the CSSF. Note that $\mathrm{PGCSSF2}_i(k) \geq \mathrm{PGCSSF}_i(k)$. Also note that all correlation metrics require common frequency vectors.

B. Error Metrics

Unlike correlation metrics, which have a geometric and vector space interpretation, error metrics assess differences of FRFs or differences of ratios of FRFs. Error metrics have their origins in the plant identification and controls communities. In SISO systems, gain and phase margins are well-known criteria for assessing the robustness of the loop transfer function. Sufficient gain and phase margins are built into the control systems to account for plant errors. The robustness of MIMO systems is often represented in terms of structured or unstructured uncertainty models and principal gains of the plant. In either case, when identified models are used in control system design, some measure of model uncertainty with respect to the actual plant is needed. In this section, three such error metrics are discussed: 1) equivalent magnitude error, 2) variants on additive uncertainty, and 3) rms error across frequency.

Some metrics require common frequency vectors; however, it is often necessary to compare FRFs that do not contain common frequency vectors. An rms error computed over frequency is one such practical error metric that does not require common frequency vectors. Because data quality metrics are not discussed in this paper, it will be our assumption that the measured data is the true representation of the plant, and that the error (uncertainty) being quantified derives from the synthesis and tuning process.

1. Equivalent Magnitude Error

The equivalent magnitude error (EME) metric is very straightforward and can be used for comparing the performance of plant identification methods. The EME is based on the complex ratio of the SISO model to the FRF data as given by

$$R_{m,n}(k) \equiv \frac{G_{m,n}(k)}{\hat{G}_{m,n}(k)}$$

The magnitude and phase error can be expressed as

$$E\_\mathrm{mag}_{m,n}(k) = abs\{20\log_{10}[|R_{m,n}(k)|]\}$$
$$E\_\mathrm{phase}_{m,n}(k) = abs\{K\left(\frac{180}{\pi}\right)\angle[R_{m,n}(k)]\} \quad (16)$$

The scaling factor is chosen to weight the relative importance of phase-matching error to amplitude-matching error. A value of $K = 0.2$ dB/ deg results in 30 deg of phase error being equivalent to 6 dB of gain error. It is convenient to combine the magnitude and phase errors into a single value vector over frequency for all channels:

$$\mathrm{EME}\,(k) = \max_{m,n}[E\_\mathrm{mag}_{m,n}(k) + E\_\mathrm{phase}_{m,n}(k)] \quad (17)$$

This metric can be integrated over the relevant frequency band(s) to yield a single number that summarizes the overall model fit error. Additionally, it is possible to define a plant identification cost function that is related to Eq. (17) (for example, see Jacques et al. [23] or Sidman et al. [24]). However, because Eq. (17) involves the maximum error over all transfer paths at each frequency, it would be an infinity norm cost function, which is very computationally expensive. In fact, MIMO plant identification using a SISO-type cost function can be very difficult. For complex systems, it is not uncommon for an identified plant to correlate very well with measured data in principal gain space, and yet have large SISO magnitude and phase errors in some channels. The fundamental, but not validated, premise behind the EME metric is that a model with sufficiently small SISO error is a good MIMO model. In the limit (as the error approaches zero) this is a sufficiently valid premise.

2. Variants on Additive Uncertainty

One can define many metrics based on the concept of the principal gains of the additive error between FRFs. These metrics are all based on unstructured uncertainty perturbations often used in the H_∞ control setting. The two discussed here are the weighted additive error (WAE) and the singular value scaled error (SVSE).

Unstructured uncertainty representations are consistent with some modern control design approaches. Often, the quantity of interest is the largest principal gain of the additive error between two FRFs. Although this may be useful in the robust control world, in plant identification, scaling often provides context and insight. A relative error, where the measured data is used as a weighting, provides context not found in absolute errors. To that end, two scaled additive errors are considered. The weighted additive error is defined as

$$\mathrm{WAE}\,(k) = \frac{\bar{\sigma}[G(k) - \hat{G}(k)]}{\underline{\sigma}[\hat{G}(k)]} \tag{18}$$

This metric is directly traceable to unstructured multiplicative perturbation models used in modern robust control methods [25]. Equation (19) shows that the WAE is a bound on the unstructured multiplicative uncertainty

$$\begin{gathered}\hat{G}(k) = G(k)[I + \Delta(k)]^{-1} \qquad \hat{G}(k)\Delta(k) = G(k) - \hat{G}(k) \\ \Delta(k) = \hat{G}^{-1}(k)[G(k) - \hat{G}(k)] \\ \bar{\sigma}[\Delta(k)] = \bar{\sigma}\{\hat{G}^{-1}(k)[G(k) - \hat{G}(k)]\} \le \bar{\sigma}[\hat{G}^{-1}(k)]\bar{\sigma}[G(k) - \hat{G}(k)] \\ \bar{\sigma}[\Delta(k)] \le \frac{\bar{\sigma}[G(k) - \hat{G}(k)]}{\underline{\sigma}[\hat{G}(k)]} = WAE(k)\end{gathered} \tag{19}$$

If the smallest singular value of the FRF data represents noise, then $\underline{\sigma}[\hat{G}(k)]$ can be replaced with the smallest nonnoise singular value. Qualitatively, WAE < 1 in the frequency range of interest indicates a good plant model. This condition implies that the additive error is smaller than the least significant, yet observable, dynamics. The error is sensitive to scale factor errors and to pure phase shifts between the two FRFs.

The significance of this metric is that it shows the size of the additive error relative to the least significant, yet measurable, dynamics of the system under test and is consistent with H_∞ control methods. It would be a good choice if the identified model were to be used in an H_∞ controller. On complex, dynamically rich structures where the dynamic range in the measured FRF matrix can be large at some frequencies, this metric often is difficult to interpret (i.e., it fails the insight criterion). Also, it tends to be large at the FRF poles and transmission zeros.

The SVSE is a more lenient criterion than the WAE, but one that still provides context for the additive error. It is defined as

$$\mathrm{SVSE}\,(k) = \max_i\left(\frac{\sigma_i[G(k) - \hat{G}(k)]}{\sigma_i[\hat{G}(k)]}\right) \qquad i = 1, \ldots, \min(M, N) \tag{20}$$

If the smallest singular value of the FRF data represents noise, the SVSE is calculated over only those singular values that represent system dynamics. The physical significance of this error is that it scales the singular values of the additive error by the measured FRF principal gains of comparable significance.

3. RMS Error Across Frequency

An rms error is often used as a cost function in plant identification algorithms. Two evaluation metrics based on the rms error are presented. The frequency rms, or FRMS, error describes the rms additive error at each frequency. It is defined as

$$\begin{aligned}\mathrm{FRMS}\,(k) &= \|G(k) - \hat{G}(k)\|_{\mathrm{Fro}} \\ &= \sqrt{\mathrm{trace}\{[G(k) - \hat{G}(k)]^H[G(k) - \hat{G}(k)]\}} \\ &= \sqrt{\sum_i \sigma_i^2[G(k) - \hat{G}(k)]}\end{aligned} \tag{21}$$

The FRMS error is consistent with plant identification techniques that identify models based on least squares error minimization. Most plant identification methods directly or indirectly synthesize a model that minimizes a cost function like the global rms error, J_{RMS}:

$$\begin{aligned}J_{\mathrm{rms}} &= \sqrt{\frac{1}{K}\sum_{k=1}^{K}[\|G(k) - \hat{G}(k)\|_{\mathrm{Fro}}]^2} \\ &= \sqrt{\frac{1}{K}\sum_{k=1}^{K}\mathrm{trace}\{[G(k) - \hat{G}(k)]^H[G(k) - \hat{G}(k)]\}} \\ &= \sqrt{\frac{1}{K}\sum_{k=1}^{K}\sum_i \sigma_i^2[G(k) - \hat{G}(k)]}\end{aligned} \tag{22}$$

It is equally applicable to SISO, SIMO, MISO, and MIMO systems. Because the FRMS metric is a function of frequency, it can be used to define frequency-weighting matrices for use in model-tuning algorithms. This metric is sensitive to scale factor errors and to pure phase shifts between the two FRFs.

Whereas the FRMS evaluates the rms error at each frequency, it is often helpful to compare the rms of FRFs across frequency. The channel rms (CRMS) error is a basic quantity intended to verify the consistency of the input and output channel gains. It is complimentary to the FRAC, which is normalized. The CRMS error is the normalized difference between the rms levels of each SISO path in the FRF matrix:

$$\mathrm{CRMS}_{m,n} = \frac{|[\int |G_{m,n}(f)|^2 \mathrm{d}f]^{1/2} - [\int |\hat{G}_{m,n}(f)|^2 \mathrm{d}f]^{1/2}|}{[\int |\hat{G}_{m,n}(f)|^2 \mathrm{d}f]^{1/2}} \tag{23}$$

The integrals take care of different frequency vectors and can be approximated with the trapezoidal method for numeric integration. Small values indicate appropriate scale factor compatibility. The metric is insensitive to pure phase shifts between the two FRFs. The individual SISO path rms levels (not just the differences) should be considered as well to identify the relative amplitudes of the SISO paths in the FRF matrix, because low response channels may be discounted by plant identification algorithms. This metric is useful for assessing effects such as frequency resolution.

V. Example 1: Correlation Metrics Applied to a Bus Simulator

The metrics described in the preceding section were used to evaluate frequency response data and identified models of two

systems with structural and modal complexity typical of spacecraft. The first structure was a dynamic simulator of a spacecraft bus. A bus is the part of the spacecraft that supports the payload, and includes wires, pipes, brackets, and structures to accommodate spacecraft subsystems and hardware for guidance, navigation, control, data handling, communications (telemetry), propulsion, power management (batteries and solar arrays), and thermal control (heaters or radiators). The bus simulator tested in this work had a mass of approximately 70 kg (∼154 lb) and was fabricated mostly of aluminum. The bus was dynamically similar to a bus for a midsized spacecraft (∼300 kg), having attached mass simulators for many subsystems and connecting cables that resulted in natural frequencies and structural damping similar to what would be found on a real bus. However, the simulator did not include propellants or any liquids, onboard computers, or solar arrays.

The bus was modally tested in a cantilever configuration (flexure boundary conditions). Four electrodynamics shakers (suspended from bungee cords) with force transducers were attached and used to excite the structure in different axes. The structural response was measured using a large array of uniaxial and triaxial accelerometers. Cables that connected the sensors to the signal conditioners and data acquisition systems were supported off the structure so that they would not dynamically load or interact with the test structure.

An initial model of the bus simulator was developed using a very detailed finite element model. From the finite element model, a reduced-order state-space model was synthesized that included 200 states and had an effective bandwidth of about 500 Hz. This model was used for the correlation analysis presented here, and included the four electrodynamic shaker force inputs and 20 accelerometer outputs (input and output channels).

The FRAC correlation metric was used to compare model-generated FRFs to measured FRFs. Figure 3 shows the MIMO FRAC, which indicates a potential problem with shaker input channel 1, as indicated by the relatively low FRAC values. The other input-output paths showed a good degree of correlation. The individual SISO responses from input 1 to sensor 1 (1/1), and input 1 to sensor 9 (9/1) are presented in Figs. 4 and 5, respectively. Both frequency response functions exhibited low signal-to-noise and correspondingly poor model fit below 8 Hz. It is unknown if the signal-to-noise issue resulted from actuator (shaker) performance, transducer (load cell) response, or some other form of signal noise. Additionally, Figs. 4 and 5 show one of the sensitivities of the FRAC; it has low values when the discrepancy is in a "high response" region. For transfer path 1/1, the FRAC value was 0.11, as a result of the amplitude below 8 Hz being large in comparison to the rest of the bandwidth. For transfer path 9/1, the model discrepancy was similar; however, the amplitude was lower than the amplitude of the rest of the bandwidth, therefore the FRAC was comparatively larger at 0.96. Figure 6 shows the MIMO FRAC calculated only using data above

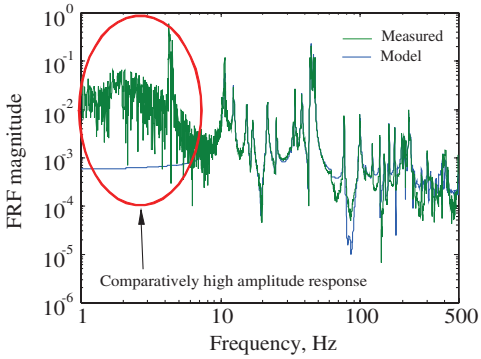

Fig. 4 SISO FRF magnitude for transfer path 1/1.

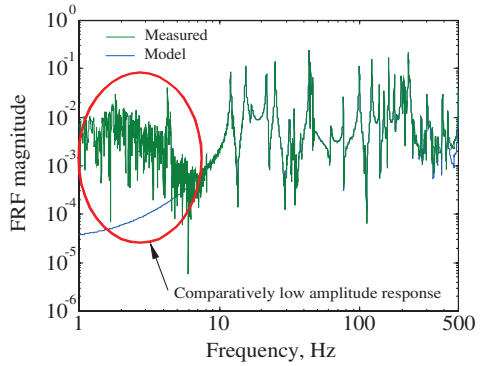

Fig. 5 SISO FRF magnitude for transfer path 9/1.

8 Hz. The results were consistently high (i.e., above 0.7) (note the change in scale). The dark blue block at 11/3 has the value of 0.73.

When the number of outputs is not too large, as is often the case in plant identification, the MIMO (row and column) CSAC and CSSF are useful for locating regions where the identified model missed mildly observable poles. However, with increasing channel count, the row CSAC becomes unwieldy and the PGCSAC and PGCSSF are more convenient. Figures 7 and 8 present the PGCSAC and PGCSSF2 for the bus simulator using four input channels and 20 output channels (therefore, four principal gain curves). The bandwidth presented has been truncated to zoom in on regions of interest. If the identified model contained all of the observable poles, then the PGCSAC plot of largest amplitude should be uniformly near unity; dips would indicate possible unidentified poles. Dips in the other PGCSAC plots may indicate unidentified dynamics as well. PGCSAC and PGCSSF2 plots showed poor correlation below 20 Hz, which was due to noisy FRF data. The dips at 34 Hz and 47 Hz

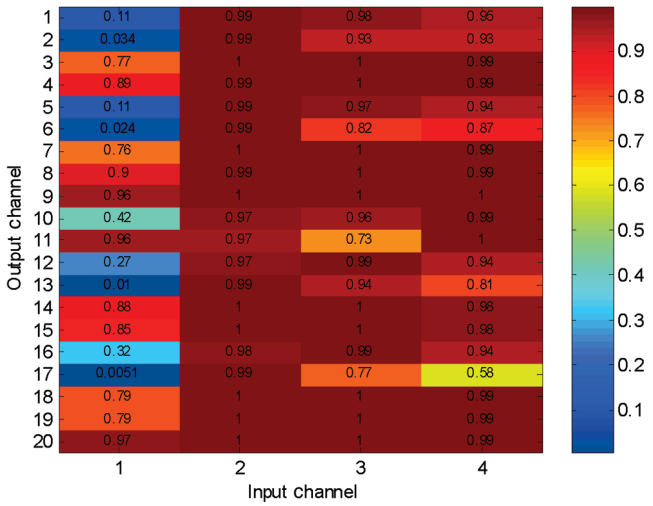

Fig. 3 Full bandwidth (500 Hz) MIMO FRAC for bus dynamic simulator.

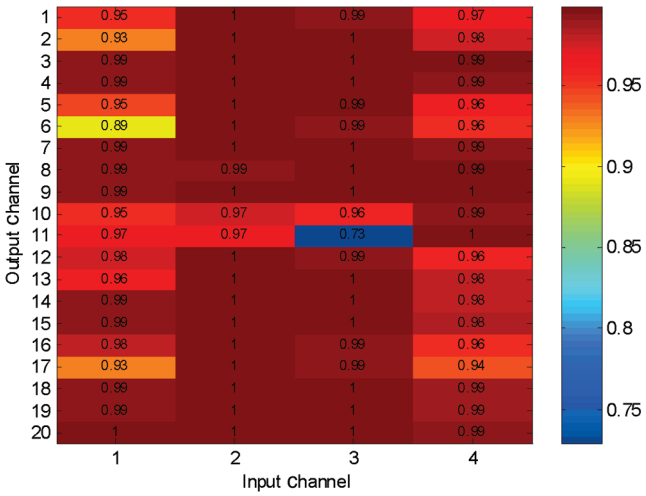

Fig. 6 MIMO FRAC for the bus dynamic simulator using data above 8 Hz only.

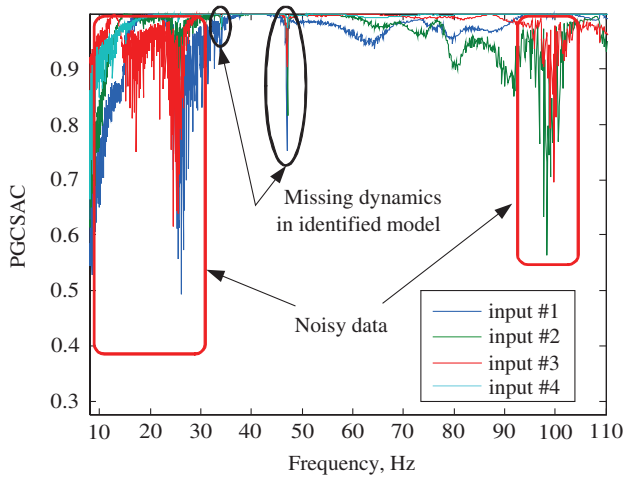

Fig. 7 PGCSAC of model and measured FRFs for the bus simulator.

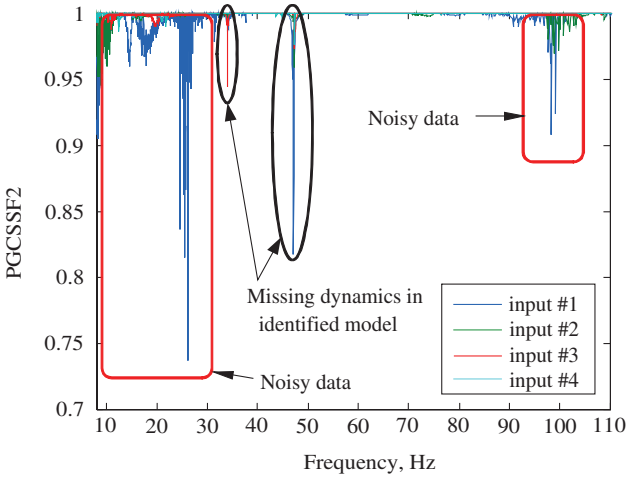

Fig. 8 PGCSSF2 of model and measured FRFs for the bus simulator.

suggest unidentified poles. To investigate, Figs. 9 and 10 show the imaginary part of two SISO measured and modeled FRFs zoomed in around 34 Hz and 47 Hz, respectively. The discrepancies indicated in Figs. 9 and 10 verify that the model missed two possible poles indicated by the data.

VI. Example 2: Error Metrics Applied to a Payload Simulator

Next, FRF error metrics were used to analyze measured data and models for a second test bed, called the deployable optical telescope (DOT), which is shown in Fig. 11. This test structure was developed

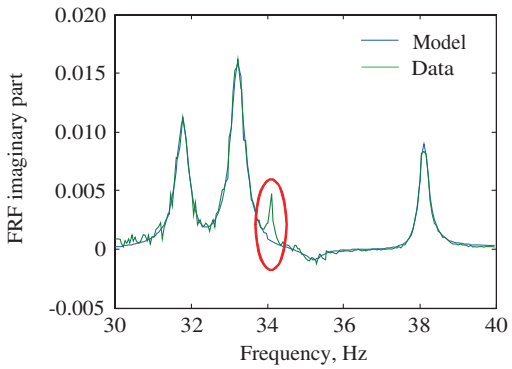

Fig. 9 Imaginary part of the measured and modeled transfer path 19/1.

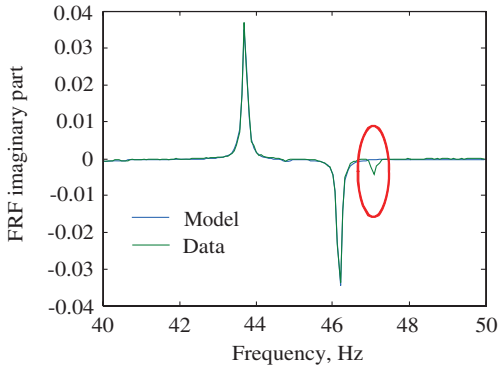

Fig. 10 Imaginary part of the measured and modeled transfer path 15/4.

by AFRL (Space Vehicles Directorate) for research on modeling and control of precision deployable optical structures. The DOT is representative of the payload side of a spacecraft. The DOT included a deployable secondary tower, a center base-hub, and three deployable petals, all fabricated from graphite-epoxy composite material. A piezoelectric patch actuator pair was attached to the base of the secondary tower to permit control of tower motion. Each petal had a single 60-cm-diam mirror fabricated from ultralow expansion glass, and was connected to the base-hub by a stiff latching mechanism. Each mirror was connected to the petals by a reaction plate with three piezoelectric stack actuators. These actuators permitted control of each mirror's piston (normal to the mirror surface), tip, and tilt motion. The mirror segments will be referred to as segments A, B, and C, and collectively constitute the telescope's primary mirror. The mirrors were pointed to a secondary mirror that was supported by a hexapod on top of the secondary tower. The base of the DOT was attached to an optics table, which was firmly bolted to the floor of the vibration-isolated laboratory. This optics table also supported a double-pass interferometry system, which provided measurements of each primary mirror's piston, tip, and tilt motion. Also observable in Fig. 11 is a white, steel metrology tower enclosing the DOT, equipped with a ladder to permit access to the secondary mirror. The metrology tower supported components of a white-light interferometer system above the DOT (not viewable in the figure).

Fig. 11 DOT solid model and structure in the laboratory.

The following analysis uses a state-space model developed from the plant identification procedure previously described in Fig. 1 (as opposed to a numerical model resulting from finite element modeling as was used in the prior example). A 334-state model was synthesized from overlapping frequency subband models (care was taken to minimize overparameterization). This model included 10 inputs (nine piezoceramic-stack actuators on the primary mirrors plus a single piezoceramic patch actuator pair on the secondary tower) and nine outputs (piston, tip, and tilt measurements from each of the three primary mirror segments), and covered a frequency bandwidth of 1000 Hz. This model was also used for design and testing of active vibration controllers to minimize motion of the primary mirror segments (i.e., disturbance rejection).

A key obstacle for plant identification on the DOT was the large amplitude discrepancy between on-segment transfer functions and cross-segment transfer functions ("on-segment" means that sensor measurements were of the mirror being actuated; "cross-segment" means that measurements were of mirrors not being directly actuated). There was a nearly 2000:1 difference in the path rms response levels in the FRF transfer matrix. Correspondingly, the first three FRF principal gains were much larger than the other six as shown in Fig. 12. Several approaches to channel scaling were investigated with varying degrees of success. Nevertheless, Fig. 12 shows that the synthesized model correlated reasonably well with data over the bandwidth, which included four decades.

In Fig. 12, there is a distinctive peak at about 10 Hz that stands apart from the other resonance peaks. This peak resulted from the lightly damped secondary tower modes. The secondary tower behaved as a cantilevered beam with a bending mode at 10.44 Hz (damping $= 0.53 \pm 0.005\%$), and a second, orthogonal bending mode at 10.85 Hz (damping $= 0.53 \pm 0.005\%$). The asymmetry resulted from the configuration of the deployment system on the secondary tower. Modeling these resonances was particularly difficult because they were so close to each other, and it was difficult to achieve the necessary frequency resolution needed for characterization. Very long data sets were required because of their long "ring-down time". The singular value scaled error is presented in Fig. 13 (only plots for the first three singular values are presented). Model error is indicated at the resonance frequencies 10 and 35 Hz. This was due in part to frequency resolution and curve-fitting of the data, but was also a result of uncorrelated excitation of the secondary tower mode during testing by ambient vibration, which introduced experimental error leading to model error. The increase in error value with frequency was an artifact of loss of signal power at higher frequencies. Diagnostically, the metric indicates that the error at the first resonance was low (less than 0.5).

Figure 14 shows WAE for the same bandwidth. As expected, it was a more stringent metric and indicated values greater than unity across the bandwidth, and peaks at the secondary tower response.

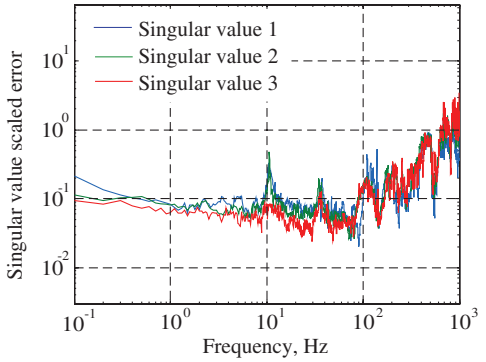

Fig. 13 SVSE of the DOT model and measured data.

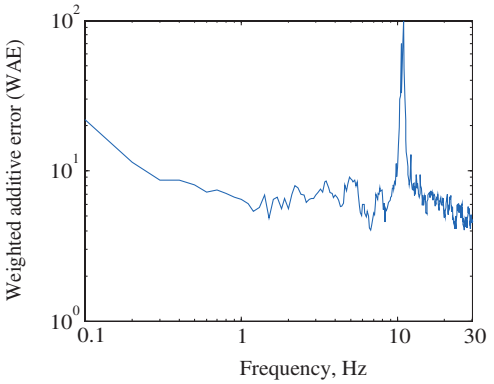

Fig. 14 WAE of the DOT model and measured data (below 30 Hz).

Based on observations of the previous figures, the WAE would serve as a reasonable bound of the model uncertainty, at least for this narrow frequency range.

Figure 15 shows the CRMS error between the model-generated and measured FRFs below 30 Hz. This highlights SISO FRF correlation, which has not been obvious in the preceding principal gain plots. Except for sensor 3 (output channel 3, the tilt sensor for mirror segment A) the model fit the data reasonably well. Diagnostically, the data would lead one to investigate output channel 3 for potential problems.

Figure 16 shows the EME for the 0–30 Hz bandwidth for the 3×3 on-segment FRF blocks, and Fig. 17 shows the EME computed for the 3×6 cross-segment FRF blocks. This was a very good metric for this region because the requirement for integral action control (used on the DOT) implies that the low-frequency model must be accurate

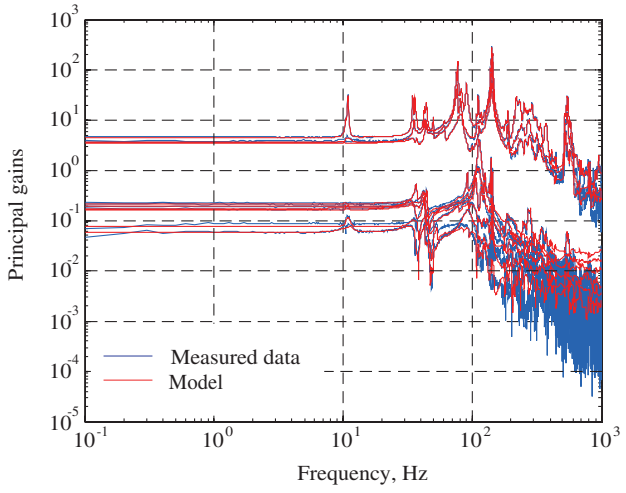

Fig. 12 Comparison of principal gains of DOT model and measured data.

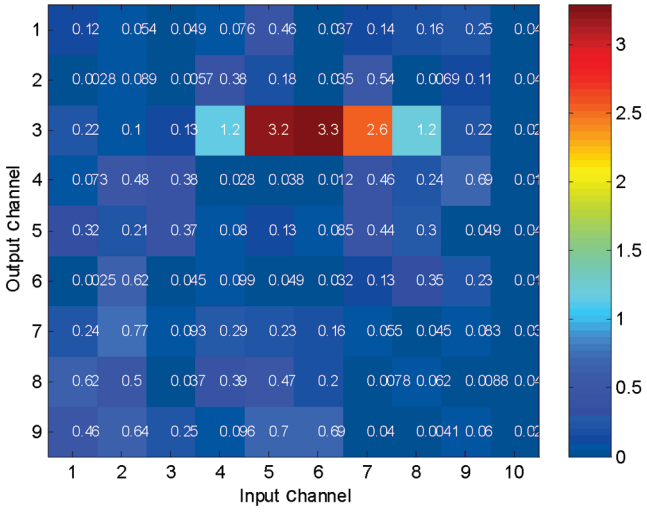

Fig. 15 CRMS error of DOT measured and model-generated FRFs below 30 Hz.

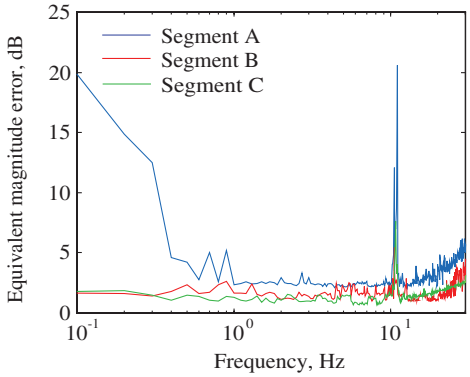

Fig. 16 On-segment EME of DOT measured and model-generated FRFs below 30 Hz.

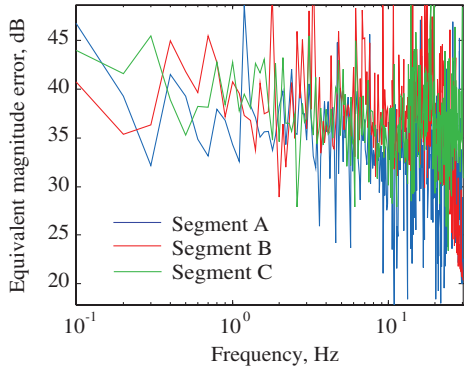

Fig. 17 Off-segment EME of DOT measured and model-generated FRFs below 30 Hz.

in all paths to avoid controller "windup" issues (accumulated displacement error). Figures 16 and 17 show that the low-frequency model error was significant for the cross-segment paths, but was low for the on-segment paths. The SNR was large at low frequencies in the cross-segment paths (i.e., it was very difficult to measure a response at one segment's sensors to a disturbance injected with a different segment's actuators). This metric gives clear indication of the degree of coupling between the primary mirror segments (i.e., it was low).

FRF measurements were collected on the DOT structure on different days (months apart) to assess the temporal stability of the structural response. The CRMS provides a convenient way to assess global differences in the measured FRF transfer matrices. Figure 18 shows the CRMS computed from two measured FRF data sets (1 kHz bandwidth). Output channels (sensors) 1, 4, and 7 were not included

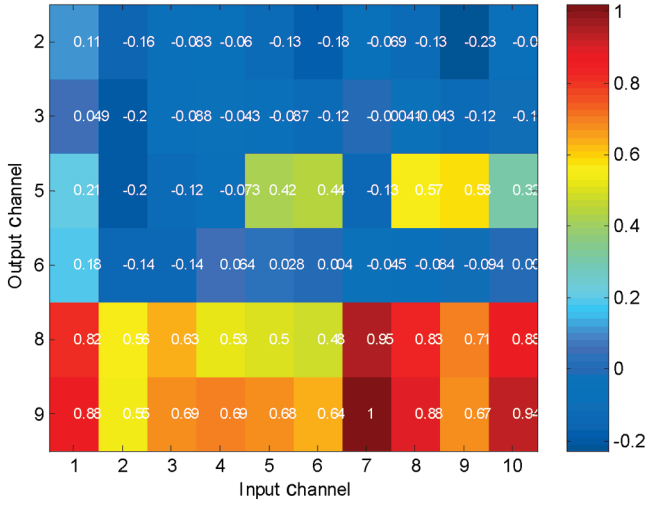

Fig. 18 DOT CRMS for FRFs measured on different days.

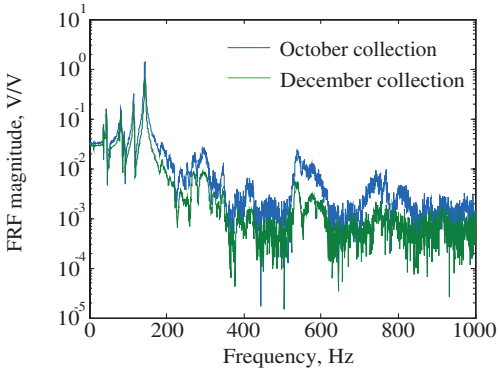

Fig. 19 DOT FRFs for path 9/7 measured on different days.

because of data dropouts (i.e., the interferometers lost lock and the data set was corrupted). The figure suggests that there were discrepancies associated with mirror segment C output channels (with which sensors 7, 8, and 9 were associated). No actuator errors were indicated by the figure, because there were no vertical strips of large error (only horizontal). The largest error was observed for transfer path 9/7. The Bode magnitude plot for this transfer path is given in Fig. 19. The data suggest a gain problem, because the magnitude difference was fairly constant across frequency.

VII. Summary and Conclusions

Correlation and error metrics are essential for accurate tuning of system models for complex structures. Analyzing data from a dynamically rich system with a large number of input and output channels can easily become intractable without the use of analysis tools to condense the data. Only through analysis of the data can one identify test-related problems such as poor signal-to-noise, failing transducers, or channel gain errors. This paper presented several correlation and error metrics that are applicable to both modal and plant identification problems. Application of the proper metrics is essential to the development of high-fidelity system models, which are requisite for controller development and performance. Correlation metrics can help quantify model uncertainty, which is necessary for robust controller design. Error metrics are useful in model-tuning algorithms used for plant identification. Each metric presented quantified the differences between models and measured data from different perspectives, and no single metric is a priori superior.

The metrics were applied to data from two representative testbeds, simulating both a spacecraft bus and payload. In both cases, these metrics facilitated analyses of large amounts of test data, and offered meaningful insight that might not be apparent by simply comparing frequency response function overlays. It was observed that the FRAC will reveal a poor fit in a high amplitude response region, but will not flag poor correlation in low amplitude regions. Furthermore, intermediate FRAC values may indicate poor correlation over a small frequency bandwidth or slight mismatches at peaks across the entire bandwidth. In a MIMO system, the MIMO FRAC reduces the data into a form that highlights potential problems and helps the engineer prioritize their assessment efforts.

The data assurance criteria (FRAC, CSAC, CSSF) all provide essentially the same information. The best MIMO extension for the given example seems to be forming a matrix of all the SISO CSAC values. The principal gain CSAC was a very good MIMO extension of the CSAC metric, although somewhat less insightful. It made identification of unmodeled dynamics easier than the other MIMO extensions.

It was demonstrated that error metrics such as the WAE can be used to provide insight regarding model uncertainty. On the payload example, the CRMS metric indicated potential channel hardware errors, such as damaged sensors. It was demonstrated that the relative coupling between subsystems can be inferred from error analysis, which can guide implementation of improved testing and measurement techniques. Application of the CRMS to two sets of

test data taken months apart facilitated quantification of changes in system dynamics and behavior over time.

Although the correlation and error metrics can provide significant insight, they are no replacement for good engineering judgment. The use of a particular metric for evaluation or as an optimization cost function should be based on the planned use of the model. Multiple metrics should be used during the plant identification process to gain maximum insight into the model's representation of the system and fit of the measured data. These metrics should be used with data quality metrics to insure the integrity of the measured data and assess potential plant nonlinearity.

Appendix: Derivation of Equations

Derivation of Eq. (7)

$$C(k) = \sqrt{[\hat{G}(k)\hat{G}^H(k)]^{-1}}[\hat{G}(k)G^H(k)]\sqrt{[G(k)G^H(k)]^{-1}} \tag{A1}$$

$$\begin{aligned}
&\hat{G}(k) = \hat{U}\,\hat{S}\,\hat{V}^H \\
&\hat{G}(k)\hat{G}^H(k) = \hat{U}\,\hat{S}\,\hat{V}^H(\hat{U}\,\hat{S}\,\hat{V}^H)^H = \hat{U}\,\hat{S}\,\hat{V}^H(\hat{V}\,\hat{S}\,\hat{U}^H) = \hat{U}\,\hat{S}\,\hat{S}^H\hat{U}^H \\
&\quad = \hat{U}\hat{S}^2\hat{U}^H \\
&[\hat{G}(k)\hat{G}^H(k)]^{-1} = (\hat{U}\hat{S}^2\hat{U}^H)^{-1} = \hat{U}\hat{S}^{-2}\hat{U}^H \\
&\sqrt{[\hat{G}(k)\hat{G}^H(k)]^{-1}} = \sqrt{\hat{U}\hat{S}^{-2}\hat{U}^H} = \sqrt{(\hat{U}\hat{S}^{-1}\hat{U}^H)(\hat{U}\hat{S}^{-1}\hat{U}^H)} \\
&\quad = \hat{U}\hat{S}^{-1}\hat{U}^H
\end{aligned} \tag{A2}$$

$$G(k) = USV^H \qquad \sqrt{[G(k)G^H(k)]^{-1}} = US^{-1}U^H \tag{A3}$$

$$\hat{G}(k)G^H(k) = \hat{U}\,\hat{S}\,\hat{V}^H(USV^H)^H = \hat{U}\,\hat{S}\,\hat{V}^HVSU^H \tag{A4}$$

$$\begin{aligned}
C &= (\hat{U}\hat{S}^{-1}\hat{U}^H)(\hat{U}\,\hat{S}\,\hat{V}^HVSU^H)(US^{-1}U^H) \\
&= \hat{U}(\hat{V}_{(:,1:M)})^HV_{(:,1:M)}U^H
\end{aligned} \tag{A5}$$

Equations (A1–A5) apply to wide matrices only (more columns than rows). There is an implicit assumption that $G(k)$ and $\hat{G}(k)$ have full row rank. Both S and $\hat{S}$ are real diagonal matrices and of the same dimension as $G(k)$ and $\hat{G}(k)$. The exponents 2 and -1 on S and $\hat{S}$ mean squaring or inverting the diagonal elements, respectively. The dependence of the singular vectors on k is implied in Eqs. (A1–A5). The derivation of Eq. (8) is analogous.

Derivation of Eq. (10)

$$\begin{aligned}
\mathrm{CSSF}_n(k) &= \frac{2|\hat{G}^H_{:,n}(k)G_{:,n}(k)|}{[G^H_{:,n}(k)G_{:,n}(k)] + [\hat{G}^H_{:,n}(k)\hat{G}_{:,n}(k)]} \\
&= \frac{2\{[\hat{G}^H_{:,n}(k)G_{:,n}(k)]^H[\hat{G}^H_{:,n}(k)G_{:,n}(k)]\}^{\frac{1}{2}}}{\|G_{:,n}(k)\|^2 + \|\hat{G}_{:,n}(k)\|^2} \\
&= \frac{2\left[\left(\frac{\hat{G}^H_{:,n}(k)}{\|\hat{G}_{:,n}(k)\|}\frac{G_{:,n}(k)}{\|G_{:,n}(k)\|}\right)^H\frac{\hat{G}^H_{:,n}(k)}{\|\hat{G}_{:,n}(k)\|}\frac{G_{:,n}(k)}{\|G_{:,n}(k)\|}\right]^{\frac{1}{2}}}{\frac{\|G_{:,n}(k)\|}{\|\hat{G}_{:,n}(k)\|} + \frac{\|\hat{G}_{:,n}(k)\|}{\|G_{:,n}(k)\|}} = \frac{2|\frac{\hat{G}^H_{:,n}(k)}{\|\hat{G}_{:,n}(k)\|}\frac{G_{:,n}(k)}{\|G_{:,n}(k)\|}|}{\frac{\|G_{:,n}(k)\|^2+\|\hat{G}^H_{:,n}(k)\|^2}{\|\hat{G}_{:,n}(k)\|\|G_{:,n}(k)\|}} \\
&= \frac{2\|\hat{G}^H_{:,n}(k)\|\|G_{:,n}(k)\|}{\|G_{:,n}(k)\|^2 + \|\hat{G}_{:,n}(k)\|^2}\left|\frac{\hat{G}^H_{:,n}(k)}{\|\hat{G}_{:,n}(k)\|}\frac{G_{:,n}(k)}{\|G_{:,n}(k)\|}\right| \\
&= \frac{2\|\hat{G}_{:,n}(k)\|\|G_{:,n}(k)\|}{\|G_{:,n}(k)\|^2 + \|\hat{G}_{:,n}(k)\|^2}\sqrt{\mathrm{CSAC}_n(k)}
\end{aligned}$$

Acknowledgments

The authors are grateful to Michael Vanik of The Aerospace Corporation for his insightful comments on the various interpretations of system identification. Mark Hopkins of Rochester Institute of Technology and Randy Van Vranken of ITT Industries Space Systems Division proposed the equivalent magnitude error metric and provided helpful details regarding its use and interpretation. The authors thank Lockheed–Martin Space Systems Company for providing frequency response function data from the bus simulator used in this paper.

References

[1] Adams, V., and Askenzai, A., *Building Better Products with Finite Element Analysis*, OnWord Press, Santa Fe, NM, 1999.

[2] Reddy, J. N., *Introduction to Non-linear Finite Element Analysis*, Oxford Univ. Press, New York, 2004.

[3] Hutton, D. V., *Fundamentals of Finite Element Analysis*, McGraw–Hill, New York, 2004.

[4] Haldar, A., and Mahadevan, S., *Reliability Assessment Using Stochastic Finite Element Analysis*, Wiley, New York, 2000.

[5] Ghanem, R., and Spanos, P., *Stochastic Finite Elements: A Spectral Approach*, Springer–Verlag, New York, 1991.

[6] Papadrakakis, M., and Kotsopulos, A., "Parallel Solution Methods for Stochastic Finite Element Analysis Using Monte Carlo Simulation," *Computer Methods in Applied Mechanics and Engineering*, Vol. 168, Nos. 1–4, Jan. 1999, pp. 305–20.

[7] Keane, A., and Price, W., *Statistical Energy Analysis*, Cambridge Univ. Press, Cambridge, England, U.K., 1994.

[8] Lyon, R. H., and Dejong, R., *Theory and Application of Statistical Energy Analysis*, 2nd ed., R.H. Lyon Corp., Cambridge, MA, 1995.

[9] Langely, R. S., and Bremner, P., "Hybrid Method for the Vibration Analysis of Complex Structural-Acoustic Systems," *Journal of the Acoustical Society of America*, Vol. 105, No. 3, March 1999, pp. 1657–71.

[10] Shorter, P., Gardner, B., and Bremner, P., "Hybrid Method for Full Spectrum Noise and Vibration Prediction," *Journal of Computational Acoustics*, Vol. 11, No. 2, June 2003, pp. 323–338.

[11] Mace, B., and Shorter, P., "Local Modal/Perturbational Method for Estimating Frequency Response Statistics of Built-up Structures with Uncertain Properties," *Journal of Sound and Vibration*, Vol. 242, No. 5, May 2001, pp. 793–811.

[12] Babuška, V., Erwin, R. S., and Sullivan, L. A., "System Identification of the SUITE Isolation Platform: Comparison of Ground and Flight Experiments," *Proceedings of the AIAA Structures, Structural Dynamics, and Materials Conference: Smart Damping and Isolation*, edited by Anderson, AIAA, Reston, VA, 2003; also AIAA Paper 2003-1642, 2003.

[13] Lacy, S. L., Babuška, V., Schrader, K., and Fuentes, R., "System Identification of Space Structures," *Proceedings of the 2005 American Controls Conference*, Vol. 4, Institute of Electrical and Electronics Engineers, Piscataway, NJ, 2005, pp. 2335–2340.

[14] Schrader, K. N., Fetner, R., Griffin, S., and Erwin, R. S., "Development of a Sparse-Aperture Testbed for Opto-Mechanical Control of Space-Deployable Structures," *Proceedings of the SPIE: Astronomical Telescopes and Instrumentation*, edited by R. Angel, Vol. 4849, Society of Photo-Optical Instrumentation Engineers, Bellingham, WA, 2002, pp. 384–395.

[15] Allemang, R. J., "Modal Assurance Criterion: Twenty Years of Use and Abuse," *Sound and Vibration*, Vol. 37, No. 8, Aug. 2003, pp. 14–23.

[16] Jacques, R. N., "On-Line System Identification and Control Design for Flexible Structures," MIT Space Engineering Research Center Rept. 11-94, May 1994.

[17] Liu, K., Jacques, R. N., and Miller, D. W., "Frequency Domain Structural System Identification by Observability Range Space Extraction," *Journal of Dynamic Systems, Measurement, and Control*, Vol. 118, June 1996, pp. 211–220.

[18] Skogestad, S., and Postlethwaite, I., *Multivariable Feedback Control Analysis and Design*, Wiley, New York, 1996, pp. 449–467.

[19] Dascotte, E., and Strobbe, J., "Updating Finite Element Models Using FRF Correlation Functions," *Proceedings of the 17th International Modal Analysis Conference (IMAC)*, Vol. 2, Society for Experimental Mechanics, St. Bethel, CT, 1999, pp. 1169–1174.

[20] Pascual, R., Golinval, J., Razeto, M., "Frequency Domain Correlation Technique for Model Correlation and Updating," *Proceedings of the 15th International Modal Analysis Conference (IMAC)*, Vol. 1, Society for Experimental Mechanics, St. Bethel, CT, 1997, pp. 587–592.

[21] Fotsch, D., and Ewins, D. J., "Application of MAC in the Frequency Domain," *Proceedings of the 18th International Modal Analysis Conference (IMAC)*, Vol. 2, Society for Experimental Mechanics, St. Bethel, CT, 2000, pp. 1225–1231.

[22] Heylen, W., and Avitabile, P., "Correlation Considerations: Pt. 5 (Degree of Freedom Correlation Techniques)," *Proceedings of the 16th International Modal Analysis Conference (IMAC)*, Vol. 1, Society for Experimental Mechanics, St. Bethel, CT, 1998, pp. 207–214.

[23] Jacques, R. N., Liu, K., and Miller, D. W., "Identification of Highly Accurate Low Order State Space Models in the Frequency Domain," *Signal Processing*, Vol. 52, No. 2, 1996, pp. 195–207.

[24] Sidman, M. D., DeAngelis, F. E., and Verghese, G. C., "Parametric System Identification on Logarithmic Frequency Response Data," *IEEE Transactions on Automatic Control*, Vol. 39, No. 9, Sept. 1991, pp. 1065–1070.

[25] Maciejowski, J. M., *Multivariable Feedback Design*, Addison–Wesley, Reading, MA, 1989.

L. Peterson
Associate Editor